Article

Spatial Analysis of Intra-Annual Reed Ecosystem Dynamics at Lake Neusiedl Using RGB Drone Imagery and Deep Learning

Claudia Buchsteiner [1,*], Pamela Alessandra Baur [1,2] and Stephan Glatzel [1,2]

1 Working Group Geoecology, Department of Geography and Regional Research, Faculty of Earth Sciences, Geography and Astronomy, University of Vienna, Josef-Holaubek-Platz 2, 1090 Vienna, Austria; pamela.baur@univie.ac.at (P.A.B.); stephan.glatzel@univie.ac.at (S.G.)
2 Vienna Doctoral School of Ecology and Evolution (VDSEE), Faculty of Life Sciences, University of Vienna, Djerassiplatz 1, 1030 Vienna, Austria
* Correspondence: a01467621@unet.univie.ac.at

Abstract: The reed belt of Lake Neusiedl, covering half the size of the lake, is subject to massive changes due to the strong decline of the water level over the last several years, especially in 2021. In this study, we investigated the spatial and temporal variations within a long-term ecosystem research (LTER) site in a reed ecosystem at Lake Neusiedl in Austria under intense drought conditions. Spatio-temporal data sets from May to November 2021 were produced to analyze and detect changes in the wetland ecosystem over a single vegetation period. High-resolution orthomosaics processed from RGB imagery taken with an unmanned aerial vehicle (UAV) served as the basis for land cover classification and phenological analysis. An image annotation workflow was developed, and deep learning techniques using semantic image segmentation were applied to map land cover changes. The trained models delivered highly favorable results in terms of the assessed performance metrics. When considering the region between their minima and maxima, the water surface area decreased by 26.9%, the sediment area increased by 23.1%, and the vegetation area increased successively by 10.1% over the investigation period. Phenocam data for lateral phenological monitoring of the vegetation development of *Phragmites australis* was directly compared with phenological analysis from aerial imagery. This study reveals the enormous dynamics of the reed ecosystem of Lake Neusiedl, and additionally confirms the importance of remote sensing via drone and the strengths of deep learning for wetland classification.

Keywords: Lake Neusiedl; reed; LTER; land cover classification; deep learning; DeepLabv3+; structure from motion; RGB; UAV; green chromatic coordinates

1. Introduction

Wetlands are of immense importance as highly valuable ecosystems intertwined with human welfare. They fulfill an indispensable function in preserving biodiversity, purifying water, enhancing resilience against storm surges, sequestering carbon, regulating microclimates, and more [1]. Reed belts in particular have ecological importance as habitats for highly specialized species and as a buffer zone for lakes and rivers. They provide an indispensable habitat for waterfowl [2] and invertebrates. Reed shoots are a food source for herbivores, and in an aquatic setting reed stands provide a spawning ground and nursery for fish [3], prevent erosion, and stabilize the strength of the bank [4]. The reed belt of Lake Neusiedl is the second largest coherent reed ecosystem in Europe after the Danube Delta, and for nature conservation reasons it is a very important habitat for many protected bird species [5]. Lake Neusiedl is a long-term ecological research (LTER) site contributing to a pan-European research network seeking to better understand the structures and functions of ecosystems (https://lter-austria.at, accessed on 5 August 2023) [6]. Remote sensing imagery is required to spatially visualize and analyze such sites and understand the effects of global changes at the local scale [7].

The following aerial image analysis studies of 1979, 2008, 2018/2019 addressed the extent of the reed belt of Lake Neusiedl. The Austrian reed belt of Lake Neusiedl was mapped as early as 1979 to study the vegetation damage and age classes of reeds through color infrared aerial photography [8]. The study of August 1979 was carried out on the basis of a three-feature classification utilizing the density, height, and vitality classes. In contrast, the reed mapping of August 2008 used a continuous stereoscopic (visual) interpretation of assigned pairs of aerial photographs (stereo pairs) [9]. Although the total reed belt area of Lake Neusiedl increased between 1979 and 2008, the reed stocks within the reed belt area decreased [9]. The authors showed that in the year 2008 around 12.5% of the total reed belt was covered by humic water. For the same aerial photographs from August 2008, the study of [10] measured 19% water coverage in the reed belt; the authors included small water areas with a spatial resolution of 0.25 m² as water. In [11], NDVI-inclusive airborne optical imaging was used in support of habitat ecological monitoring of the Austrian reed belt in a study investigating the different reed classes and habitat-specific dependencies of different bird species. The reed belt coverage is clearly higher in the Hungarian part of Lake Neusiedl (83.6% in 2007, which included grassland with reed coverage of around 5%) as compared to the Austrian part (around 50%). The Hungarian reed belt area decreased slightly, by 0.8% from 1979 to 2007, due to the increase in "feltöltés" (embankment/levee areas), though not in open-water areas [12]. In 2007, only 1.2% of the Hungarian part of Lake Neusiedl was covered by humic water [12], which is a very small share compared to the Austrian reed belt; see [10]. Márkus et al. [12] recognized a strong degradation of the Hungarian reed belt due to damage caused by the harvesting machines, which were called die-back sites in [13]; these were observed in the Austrian part, though to a lesser extent, in [9]. One study from 2018/2019 used Sentinel-2b data to monitor the age of reed stands, finding that the dominant age class (especially in the eastern reed belt) was areas older than 14 years [5].

Previous studies analysing the spatial patterns of the reed belt have been based on either low-resolution satellite data or medium-resolution aerial imagery derived from costly single-flight surveys. To date, the spatial patterns of the reed belt have not been studied with high-resolution data. In addition, little is known about the temporal dynamics of the surface structure of the reed belt within a one-year time frame. To address this gap, in this study we used an unmanned aerial vehicle (UAV) to generate a time series of high-resolution aerial imagery data. A series of ten UAV-derived orthomosaics provided the basis for land cover classification and phenological analysis to track changes in intra-annual variability in the spatial dynamics of the reed ecosystem over the growing season of 2021, which is of particular interest due to the intense drought during the study period. The region of Lake Neusiedl has been facing drought conditions since the summer of 2015, causing the average water level of the lake to decrease, especially in recent years [14].

The main objectives of this work are:

- To provide a detailed workflow for land cover classification of high-resolution orthoimagery using deep learning image segmentation.
- To reveal the spatial and temporal variability of a reed ecosystem under intensive drought conditions.
- To disclose the phenological stages of *Phragmites australis* in the reed stands of Lake Neusiedl over the 2021 vegetation period.

2. Materials and Methods

2.1. Study Area

The study area is located in the reed belt of Lake Neusiedl near Illmitz in Austria (47°46′09″N, 16°45′30″E). With a maximum area of 315 km², Lake Neusiedl is Austria's largest lake, stretching across the Austrian–Hungarian border. It is characterised by a remarkably shallow lake basin (Z_{mean} = 1.2 m, Z_{max} = 1.8 m) with no natural outflow [15]. The lake water has an alkaline and subsaline character [16], with high electrical conductivity (1300–3200 μS cm^{-1}) and an average pH of 8.7. The mean annual precipitation sums between 1971 and 2020 measured from eight stations surrounding the lake were 556 mm,

and ranged from 353 mm to 833 mm [14]. Due to the relatively small catchment area of the lake, rainfall contributes 79% to the total water supply via direct input through the lake surface. The lake's shallowness and expansive water surface area make it particularly sensitive to climatic variations [17].

More than half of the lake (about 181 km²) is covered by a reed belt, which consists of a temporally changing mosaic of reeds (*Phragmites australis*), water, and sediment patches. The lake and its reed belt belong to various protected areas, including the Austrian–Hungarian national park Neusiedler See–Seewinkel/Fertő, a Ramsar site and Natura 2000 area.

This study focused on an area of approximately 53 ha in the eastern reed belt of Lake Neusiedl; the study area extends from sparsely vegetated shores (landwards) to densely vegetated areas near the open lake surface. The area surveyed in the UAV flights was about twice the size of the actual study area (as shown in Figure 1) in order to achieve proper rectification and georeferencing results for the aerial images within the study area. The research area is located in the nature zone of the National Park Neusiedler See–Seewinkel, where no management is conducted and access restrictions apply. An Eddy Covariance (EC) tower for measuring greenhouse gas exchange is located in the center of the study area (https://wetlands.univie.ac.at, accessed on 5 August 2023). Several channels lead through the research area and a constructed dam pathway runs through the middle of the study site, crossing the reed belt from the land shore to the open water area.
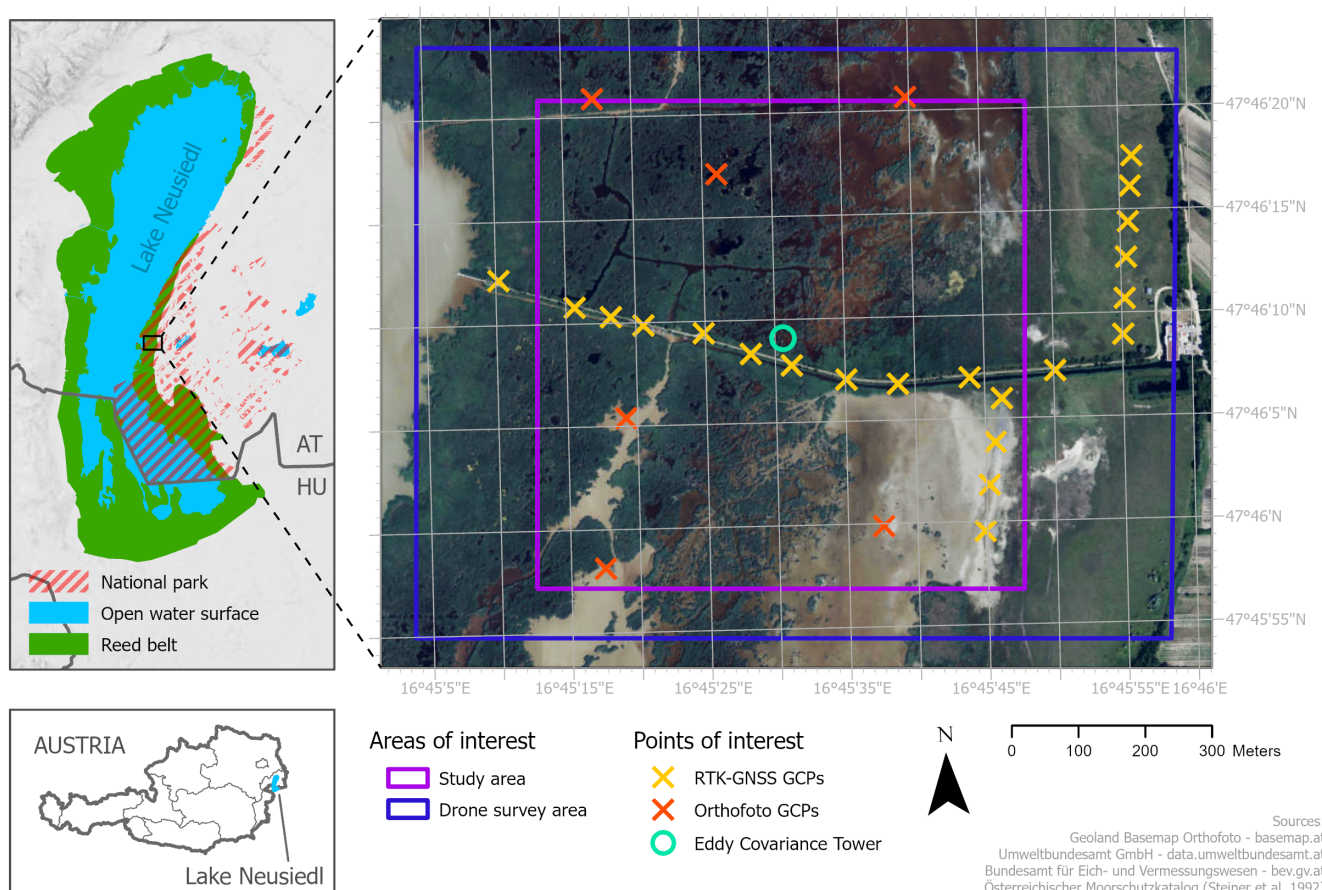
Figure 1. Overview maps and detailed map of the research area in the reed belt of Lake Neusiedl, Eastern Austria (data source used in the overview map: [18]).

2.2. Data Preparation

2.2.1. UAV Data Acquisition

High-resolution images were captured using a quadcopter drone (Mavic 2 Pro, DJI Technologies Co., Ltd., Shenzhen, China) equipped with a CMOS sensor that captures optical images in RGB with a resolution of 5472 × 3648 pixel (20 MP). The camera has a focal length of 10.3 mm and a sensor width of 12.8 mm [19]. A total of ten flight campaigns were conducted at three-week intervals, starting on 5 May and ending on 6 November 2021 (dates listed in Table 1). Because very few land cover changes in the study area's surface were expected during winter to early spring, no flights were carried out from December to April. The capacity of the four drone batteries covered an average drone survey area of 96 ha during each flight campaign (Table 1), lasting about 2.5 h each. Because distortion can occur at the edges of a processed orthomosaic, we extended the drone survey area well beyond the actual study area used for analysis (see Figure 1). In order to have as little shade as possible in the captured images, all flights were carried out at midday when the sun was at its highest. Because alternating sunny and cloudy weather conditions were to be expected over the duration of a flight campaign, the camera settings (ISO values, shutter speed and aperture) were set to automatic mode during the flights to prevent blurring and/or overexposure in the images. More than 1000 aerial images were generated during each flight campaign, with a mean data volume of 15 GB. All flights were performed in automatic flight mode with predefined parallel flight lines at a constant height of 100 m above the ground and an image front and side overlap of 75%, with all images taken at 90° to the surface (nadir). Flight plans were created using the flight planning app PIX4Dcapture, version 4.10.0 (Pix4D S.A., Prilly, Switzerland).

Table 1. Results and uncertainty values from processing orthomosaics with structure from motion (SfM) techniques.

Flight Campaign	Average GSD [1] [cm]	Drone Survey Area [km²]	RMSE Georeferencing (*N* = 21)		RMSE Check Points (*N* = 6)	
			X Error [cm]	Y Error [cm]	X Error [cm]	Y Error [cm]
2021-05-05	2.43	0.84	4.6	2.9	2.0	5.9
2021-05-26	2.39	0.92	23.9	11.7	3.2	3.6
2021-06-18	2.50	1.02	11.6	4.9	1.9	4.4
2021-07-07	2.49	0.99	24.2	8.9	10.7	5.0
2021-07-27	2.45	0.99	14.3	3.0	1.7	4.9
2021-08-18	2.41	0.99	15.5	10.2	3.9	4.2
2021-09-10	2.45	0.95	6.8	3.1	4.5	5.8
2021-09-29	2.36	0.97	5.2	3.8	3.8	5.2
2021-10-20	2.36	0.94	8.3	28.7	2.7	6.0
2021-11-06	2.32	1.00	3.0	1.4	3.2	5.6
Average	2.42	0.96	11.7	7.9	3.8	5.1

[1] Ground sampling distance.

2.2.2. Photogrammetric Preprocessing

To georeference the drone imagery, 21 ground control points (GCPs) with a chessboard pattern in DIN-A3 format were produced and distributed in the study area (displayed with a yellow x in Figure 1). To ensure their durability over the duration of all flight campaigns, the GCPs were laminated with a strong and UV-resistant film and fixed to wooden boards before attaching them to driven wooden piles and existing fence posts. Fixing the GCPs on posts above ground guaranteed their visibility to the drone sensors throughout the vegetation period. A GNSS receiver (Trimble R10, Trimble Inc., Sunnyvale, CA, USA) was used for precise location measurement of the GCPs [20]. In addition, RTK-based correction using the Austrian Positioning Service (APOS) was applied to improve the precision of the measurements.

To obtain distortion-free image processing results, the GCPs were distributed evenly over the study area [21]. Due to access restrictions in the National Park covering the study area, our original idea of deploying GCPs along the water channels of the study site could not be implemented, as this was considered a potential disturbance factor for breeding birds. For this reason, GCPs were densified along the dam pathway and along the land shore line of the reed belt, where temporary entry was permitted. The area of the drone survey had to be extended in the easterly direction in order to capture the easternmost GCPs with the drone sensor. Furthermore, an additional set of control points (displayed with a red x in Figure 1) was derived from an orthophoto (2019-06-26, resolution 20 cm) obtained from the Austrian Federal Office of Metrology and Surveying (BEV) [22] by manually locating the center of small, isolated, and uniquely identifiable reed patches.

The image datasets from each flight were processed to a rectified and georeferenced orthomosaic using the Structure-from-Motion (SfM) image matching technique, which is widely used in geoscience applications [23] and described in detail by Deliry and Avdan [24]. This preprocessing workflow was carried out using the photogrammetry software PIX4Dmapper, version 4.6.4 (Pix4D S.A., Prilly, Switzerland) according to the instructions [25]. Processing options such as the image scale at which key points were computed or the degree of camera optimization were adapted to the individual requirements of each flight dataset. In SfM processing, GCPs must be manually marked in different images captured from different angles. Identifying the same geolocation in the small isolated reed patches of the six orthophoto-derived control points was more challenging than identifying the center of the RTK-GNSS measured chessboard-patterned wooden boards designed for accurate marking. Of the 27 available control points, 21 were used for rectifying and georeferencing, while the remaining six served as check points to verify the accuracy of the resulting orthomosaics (results shown in Table 1). The control points derived from the orthophoto were not used as check points, as check points were not included in the process used to rectify the orthomosaic and would have caused wide areas with distortion of unknown extent. The average ground sampling distance (GSD) across all flights was 2.42 cm/pixel. The RMSE (root mean square error) of the control points used for georeferencing was 11.7 cm in the X and 7.9 cm in the Y direction; while relatively high compared to the GSD, this is acceptable considering the size of the covered area. Both the lower resolution of the orthophoto and the inherently less accurate method of identifying the center of the reed patches resulted in significantly higher uncertainty values for georeferencing than we initially aimed for (see Table 1). Because only RTK-GNSS-measured GCPs were used as control points, their significantly lower uncertainty values apply only along the areas of their spatial distribution. The computationally intensive procedure of photogrammetric processing was performed on an Intel(R) Core(TM) i7-10700 CPU @ 2.90 GHz with 32 GB RAM (Intel Corporation, Santa Clara, CA, USA) and a Radeon RX 550X GPU (AMD Inc., Santa Clara, CA, USA).

2.3. Semantic Segmentation

In this study, we used semantic image segmentation for classifying the different land cover types of the study area. Semantic segmentation is a machine learning technique that assigns a class label to each pixel in an image [26]. The whole workflow, from generating training data for deep learning to model training and pixel classification, was carried out in ArcGIS Pro 3.0.3 [27] with the Image Analyst license and Deep Learning Libraries for ArcGIS Pro 3.0.3 [28]. Figure 2 illustrates the most important processing steps carried out for each orthomosaic, which are described in detail as follows. (a) Deriving ground truth data: from each orthomosaic, a subset of eight square areas (referred to henceforth as "ground truth areas") covering 2500 m² each was obtained. The ground truth areas were carefully selected to cover the various characteristics of the land cover classes, such as their structure and colour expression. Care was taken to ensure that the transition zones between classes (water to sediment, water to vegetation, and sediment to vegetation) were represented within the ground truth imagery. (b) Image annotation: for each of the eight ground truth

areas, a fully labeled layer was generated using a semi-automated workflow. A detailed description of the procedure can be found in Section 2.3.1. (c) Construction of a chip dataset for deep learning: a dataset consisting of image chips and analog labels was derived from the fully labeled ground truth data. All chips were exported in TIFF format with a size of 256×256 pixels and a 50% overlap both horizontally and vertically. The chip dataset was cleaned to remove chips containing areas without any information. This processing step yielded an average of 1641 chips and the same number of corresponding labels per dataset. (d) Training a deep learning model: the chip dataset was used to train and validate a deep learning model. A detailed description of the procedure can be found in Section 2.3.2. (e) Semantic segmentation for classifying land cover types of the reed belt: the trained model was finally used to assign a semantic class label to each pixel of the respective orthomosaic using the "Classify Pixels Using Deep Learning" tool in ArcGIS Pro. The dam pathway and a boat pier were generously cut out of the classified data used for further analysis.
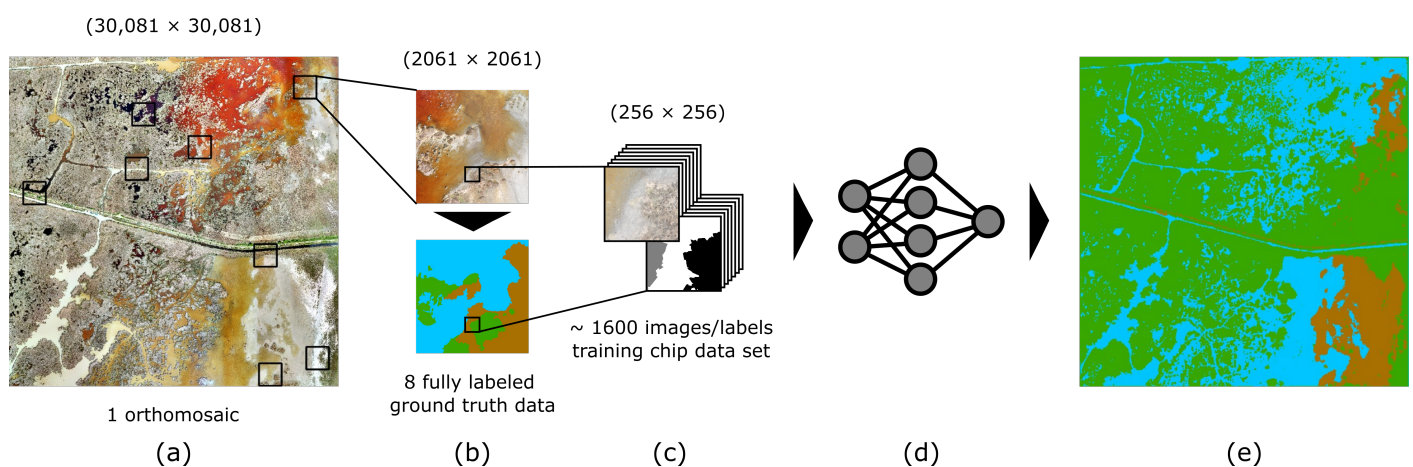
Figure 2. Full workflow for classifying different land cover types in the reed belt through semantic segmentation. The different stages of data processing are shown with the respective image size in pixels. (**a**) Orthomosaic of the study area (from flight 2021-05-05), with selected locations for ground truth areas. (**b**) Image annotation data, consisting of ground truth imagery and a fully labeled layer indicating the corresponding land cover classes (vegetation = green, water = blue, sediment = brown). (**c**) Chip dataset containing small image chips and analog labels derived from ground truth data. (**d**) Training and validation of a deep learning model with the training chip dataset. (**e**) Semantic segmentation performed on the orthomosaic using the trained model.

2.3.1. Image Annotation

The process of generating ground truth data is known in the machine learning domain as image annotation. A number of image annotation programs have recently become available, although most of them are proprietary. With the aim of preparing ground truth data at no additional cost and with maximum control over the parameter settings, a standardized semi-automated workflow for image annotation was developed within the ArcGIS Pro environment using the segmentation tool for object based image analysis (OBIA). For each of the ten orthomosaics, a ground truth dataset was prepared as follows (the individual steps are shown in Figure 3):

(a)   The eight carefully selected ground truth areas were clipped from the orthomosaic and resampled to a resolution of 10 cm using the bilinear resampling technique. Resizing of the imagery was done to reduce processing time for the next step.

(b)   The resampled imagery was segmented into groups of adjacent pixels with similar spectral characteristics. The segmentation tool within the software can be used to define the spectral and spatial detail. It was found that the best segmentation results for distinguishing between the classes in our data were obtained when the spectral detail was set between 15 and 17 and the spatial detail set to 1. Furthermore,

the minimum segment size was set to 500 pixels. With these parameter settings, while the segmentation algorithm produced fragmented patches that were smaller then required, it provided proper delineation between land cover classes along certain segment boundaries.

(c) The raster output from the segmentation tool was vectorized for the next processing step.

(d) Segments from the same semantic classes were manually merged. Merging was performed by visual interpretation of the polygons while overlaying the ground truth imagery. To speed up this process, segments smaller than 1 m² were removed and the resulting gaps were filled by adding the geometry of the gap to the adjacent polygon with which it shared the longest edge. This step provided fully overlapping semantic class polygons, with each polygon covering the entire area of a class along with its various intra-class variations contained in the ground truth imagery.

(e) As a last step, the polygons were assigned to the corresponding land cover class in order to obtain a fully labeled polygon layer.

Steps (a) through (e) were repeated for the eight selected ground truth areas from each of the ten orthomosaics. The ground truth imagery in original resolution and the corresponding fully labeled polygon layer were used as input data for exporting the training chips dataset.
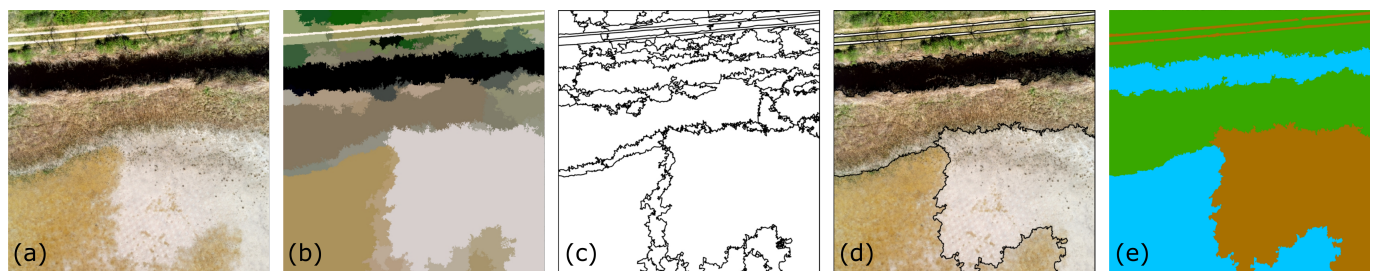
Figure 3. Workflow example of image annotation from one selected ground truth area. (**a**) Clipped and resampled ground truth imagery covering various characteristics of vegetation, water and sediment. (**b**) Segmentation output showing adjacent pixel groups with similar levels of spectral detail. (**c**) Segmentation raster converted into polygons. (**d**) Polygon segments merged by visual interpretation. (**e**) Fully labeled polygon layer for respective ground truth imagery, showing the land cover classes of vegetation (*green*), water (*blue*), and sediment (*brown*).

2.3.2. Deep Learning

A deep learning model was trained with each chip dataset using a deep convolutional neural network (CNN) architecture for image segmentation. With the rise of deep learning, CNNs have been applied for various land cover classification applications on high-resolution remote sensing data [29–31]. In this study, we used the state-of-the-art DeepLabv3+ model architecture, which uses an encoder–decoder framework with atrous convolution and a variant of the Xception network as its backbone [32]. This model proved to be highly accurate in wetland classification on high-resolution RGB imagery [33,34].

The chip datasets were split into 80% training and 20% validation data and stratified in order to maintain the class proportions between the training and validation data. The optimum learning rate for the model training was determined for each chip dataset (see Appendix A). Pre-testing revealed that the model's accuracy was saturated after 20 to 30 epochs. With the intent of making the results more comparable, we trained each model for 25 epochs. Several performance metrics were calculated at the land cover class level to evaluate the accuracy of the models. Precision (1), Recall (2), and F1-Score (3) were calculated as standard evaluation metrics for machine learning models. In addition, Intersection over Union (IoU), which is a standard measure for semantic image segmentation, was calculated using Equation (4) [35]. In contrast to the other metrics, IoU uses the entire ground truth map instead of labeled points to assess the similarity between the predicted

and the ground truth map for a given class. This performance metric is progressively being applied in deep learning-based UAV remote sensing classification [30,34,36,37].

Formulas for the above-mentioned metrics are provided in Equations (1)–(4), where true positive (*TP*) represents the count of correctly labeled pixels, false positive (*FP*) refers to the count of pixels misclassified as the target class while belonging to other classes, and false negative (*FN*) refers to the count of pixels that belong to the target class and are misclassified as belonging to other classes.

$$Precision = \frac{TP}{TP + FP} \tag{1}$$

$$Recall = \frac{TP}{TP + FN} \tag{2}$$

$$F1\text{-}Score = 2 * \frac{(Precision * Recall)}{(Precision + Recall)} \tag{3}$$

$$IoU = \frac{TP}{FP + TP + FN} \tag{4}$$

Model training was carried out on an ArcGIS Notebook (integrated Jupyter Notebook, version 5.7.10) with the *arcgis.learn* module included in ArcGIS API for Python 3.9.11 [38]. The training took about one hour per model and was performed on an Intel(R) UHD Graphics 630 GPU (Intel Corporation, Santa Clara, CA, USA) with NVIDIA Quadro T2000 (Nvidia Corporation, Santa Clara, CA, USA).

2.4. Phenological Analysis

A vegetation index was calculated with the aim of tracking phenological stages over the vegetation period within the study area. We extracted the vegetated areas of each orthomosaic using the results from the land cover classification. For these areas, the Green Chromatic Coordinates (GCC) vegetation index was calculated from the red–green–blue (RGB) colour channel information using the formula in Equation (5). Of the various vegetation indices available for RGB data, we chose GCC due to its effectiveness in suppressing changes in scene illumination [39], which occurred in several orthomosaics.

$$GCC = \frac{G}{R + G + B} \tag{5}$$

Phenocam Data

In the center of the study area, a digital camera (Powershot SX620 HS, Canon Inc., Tokyo, Japan) was positioned at the Eddy Covariance tower (see Figure 1) in the main wind direction (north–west) to study the phenological changes of the reed plant *Phragmites australis* since September 2020. The Phenocam automatically takes an RGB image every 1 h from 6 am to 5 pm (time zone UTC + 1), which was ensured by manipulation with the Canon Hack Development Kit (CHDK). The photos were analyzed with the R package *Phenopix* [40]. For this study, one polygon as region of interest (ROI) was drawn in the reference picture to study the temporal changes of *P. australis* in the entire year 2021 (see Figure 4). For the ROI, the GCC vegetation index was extracted using an ROI-averaging approach [41]. GCC values were filtered according to the *max* approach following [39] after determination of the 90th percentile values in three-day moving windows, as this filter effectively minimized the impact of lighting changes in the environment.

Processing and statistical analysis of the Phenocam data were carried out using R (Version 4.1.2, [42]). For faster data processing, the R package *data.table* was used [43]. The R package *ggplot2* was used to visualize the results [44].

Figure 4. The region of interest (ROI) is marked as a black polygon in the reference picture 2021-06-23 of the Phenocam, which is aligned at the Eddy Covariance tower in the reed belt of Lake Neusiedl in the main northwest wind direction.

3. Results

3.1. Performance Metrics

Performance evaluation of deep learning models was based on the accuracy metrics Precision, Recall, F1-Score, and IoU. The Precision, Recall, and F1-score achieved mean results above 90% over all class types, with a small deviation in the maximum SD of 2.7% (see Table 2). The vegetation class scored particularly highly on these metrics, with noticeably low deviation. The IoU reached mean results ranging from 68.5% to 89.9%, showing higher variance within the class types. The vegetation class again performed the best of all classes. The sediment class type achieved a mean IoU of 72.0% with an SD of 8.1%, and the water class type reached a mean value of 68.5% with a comparably high variance of 11.5% SD. Detailed information on the models' accuracy metrics can be found in Appendix A.

Table 2. Performance metrics of deep learning models ($N = 10$) trained for land cover classification of UAV [1] imagery tracking the reed ecosystem from May–November 2021. Metrics are represented with mean values ± SD [2] of trained models at the class level. The full table is provided in Appendix A.

Class	Precision	Recall	F1-Score	IoU [3]
	Mean ± SD	Mean ± SD	Mean ± SD	Mean ± SD
Vegetation	0.958 ± 0.010	0.957 ± 0.007	0.958 ± 0.006	0.899 ± 0.020
Water	0.929 ± 0.026	0.923 ± 0.024	0.925 ± 0.020	0.685 ± 0.115
Sediment	0.918 ± 0.023	0.927 ± 0.027	0.922 ± 0.020	0.720 ± 0.081

[1] Unmanned Aerial Vehicle, [2] Standard Deviation, [3] Intersection over Union.

3.2. Land Cover Classification

Area shares of the the three land cover class were calculated from each orthomosaic ($N = 10$). Figure 5 shows the spatial and temporal variability of land cover in the study area within the study period of May to November 2021.

The majority of the study area is covered with vegetation (60.8% to 70.9%), and vegetation has the lowest variation of all the class types over the entire study period. The vegetated area showed a rapid increase from May to mid June (+6.6%). After a sudden vegetation decline at the beginning of July (−2.7%), a steady increase began, peaking at the end of September (+6.2%). Thereafter, the vegetation class remained almost stable, with a slight decline until November (−0.3%). The area shares of water and sediment have an interdependent relationship, and show similar variations, although their area shares differ. Water had its maximum surface coverage in May (29.9% and 30.2%), when sediment showed its minimum extent (9.3% and 6.3%). Within two months, a strong decline in the water class (−25.2%) caused sediment to reach its maximum extent (29.4%) at the end of

July. In August, the water area increased slightly before declining to its minimum extent at the beginning of September (3.3%). From the end of September to November, the respective shares of water and sediment areas fluctuated at a very low level, with maxima of ±0.5% and ±0.7%, respectively.

The changes in the spatial distribution of land cover classes during the study period are shown in the land cover classification maps in Appendix B. An increase in vegetation area was observed along the edges of existing reed stands. For this reason, the water channels became increasingly overgrown with *Phragmites australis* during the study period, as can be seen in the maps. In addition, densification of loosely vegetated areas was observed from early May to late September. The land cover development in the study area shows a constant and large increase in sediment area from the land shore side combined with a large decrease in water area from end of May to end of July 2021. Moreover, the maps show a rather stable spatial distribution with minimal changes in land cover from the end of September to the beginning of November.
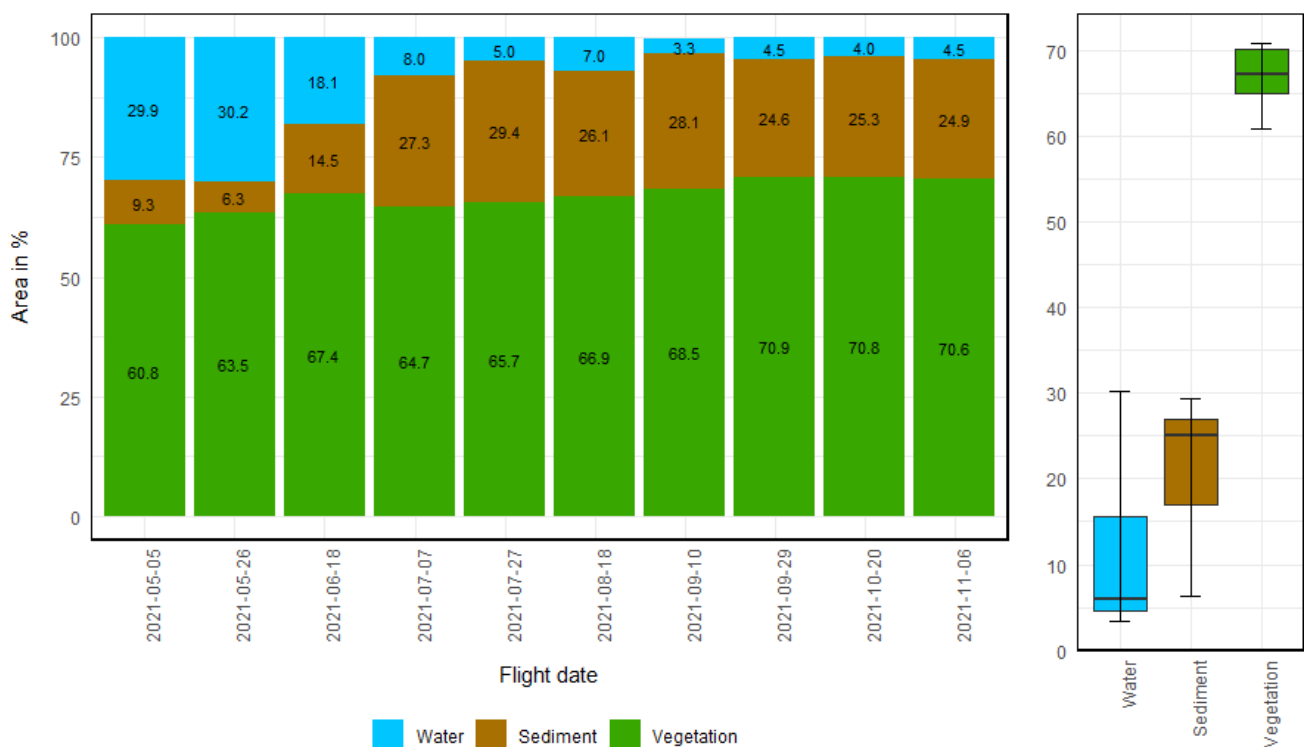
Figure 5. Spatio-temporal variability in the study area of Lake Neusiedl's reed belt from May–November 2021.

3.3. Vegetation Index

The seasonal course of vegetation development during the study period could be observed based on the orthomosaics of our study area. For better understanding of phenological development, GCC values were calculated for each pixel of the vegetated areas. The seasonal course of vegetation phenology in the entire vegetated study area is presented as the mean ± SD of the GCC value pixel counts, and can be seen in green in Figure 6. In the study period, the mean values of GCC ranged between 0.33 to 0.40. The vegetation areas showed an increase in GCC values from early May until late July, when it peaked. Thereafter, the mean GCC values decreased and remained stable at 0.37 until the end of September, continuing to decrease until again reaching the baseline value from early May (0.33) in November.
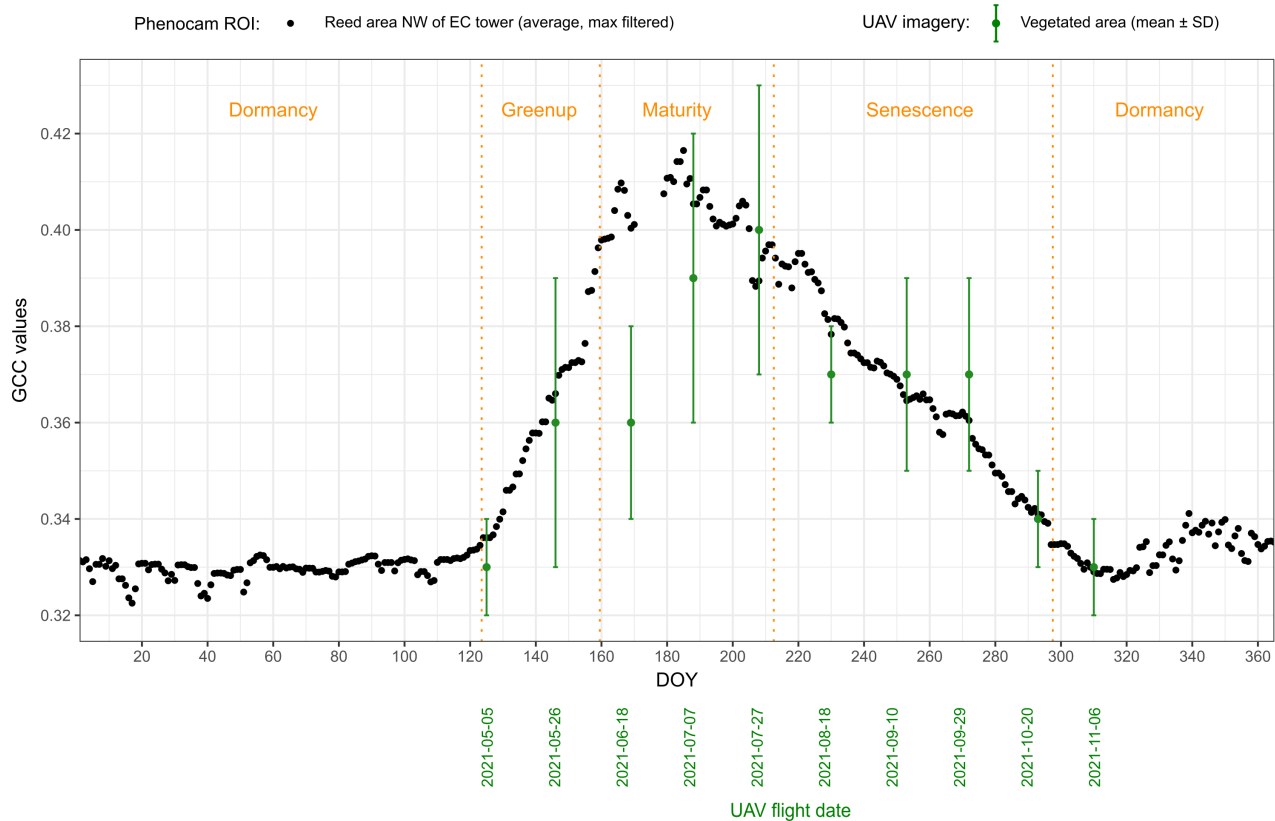
Figure 6. Comparison of the seasonal course of vegetation phenology (year 2021) between the ROI of the phenocam data and the study area covered by the UAV imagery using the GCC vegetation index. The GCC values of the Phenocam ROI (black dots) show the average phenology of the reed stands at the Eddy Covariance tower in the NW direction (center of the study site) for almost every day of year (DOY) in 2021 as compared to the mean ± Standard Deviation (SD) of the GCC values calculated from the ten UAV flights (green dots with error bar) for the entire study site covering the land to the open water shore of the reed belt. The phenology stages of the Phenocam data are separated by the orange dotted lines.

The GCC maps in Appendix B reveal the spatial and temporal heterogeneity of the phenological development within the vegetated areas. At the beginning of the study period, the GCC values increased along the edges of existing reed stands and in loosely vegetated areas. In areas of dense vegetation, the GCC values gradually increased until the end of July, though they did not reach the maximum in the most densely vegetated areas. The GCC histograms in Appendix B differ in width and height. A narrow distribution of GCC values indicates more homogeneous status of the reed stands (e.g., 2021-05-05), while a wider distribution shows heterogeneity of reed shoot development within the reed stands (e.g., 2021-07-27).

The Phenocam provided us with the opportunity to study the phenological changes of the reed stands of *P. australis* to the northwest (the main wind direction) of the EC tower located in the center of the study area on a daily basis. The trend of the GCC values of the Phenocam in 2021 are shown together with the mean ± SD GCC values of the UAV flights in Figure 5. From January to the beginning of May, the GCC values of the Phenocam were stable at 0.33 (phenology stage *Dormancy*). The GCC values started to increase in the beginning of May 2021 (DOY 124). The phenology stage *Greenup* ranged until the beginning of June (DOY 159). The phenology stage *Maturity* started at DOY 160, with the highest peak at the beginning of July (DOY 177) with 0.42. The *Senescence* phenology stage started at the beginning of August (DOY 213). The GCC values decreased to 0.33 until the end of October (DOY 298), then slightly increased in the *Dormancy* phenology stage to 0.34 at the end of

the year 2021. According to the GCC values of the Phenocam data, the vegetation period of the reed stands next to the EC tower in 2021 was around 173 days (4 May until 24 October).

4. Discussion

Changes in the land cover and phenological stages of the reed belt of Lake Neusiedl were investigated and identified using ten study dates in the period between 5 May 2021 and 6 November 2021. Land cover classification was performed using deep learning image segmentation, while phenological analysis were carried out using the GCC vegetation index. As a basis for these analyses, SfM-derived orthomosaics generated with high-resolution RGB drone imagery were used. Furthermore, we have provided the detailed workflow used in generating the fully labeled ground truth data for training and validation of our deep learning model.

Due to access restrictions, GCPs could not be evenly distributed within the study area as recommended [21]. In order to obtain comparable SfM results and derived subsequent land cover classifications, it was necessary to acquire additional control points from an orthophoto. This solution led to a higher RMSE than was initially targeted in terms the uncertainty values of the SfM processing; however, this was accepted due to the lack of alternatives and can be considered sufficient as compared to the existing literature [24]. Considering the access restrictions imposed by the National Park, the minimally invasive method of UAV surveying is currently the most feasible way to collect data covering large areas with this level of detail, despite the constraints around GCP distribution.

One of the biggest challenges anticipated in our study involved the different appearance of the surface of the study area throughout the investigation period due differences in the sunlight conditions between flights. As can be seen from Figure 3 and Appendix A, even within a single orthomosaic the study area showed strong variations within classes; e.g., water could range from crystal-clear to opaque turbid due to the sediment load, and had different color expressions, while certain inter-class expressions such as dry sediment and dead reeds hardly differed. Our attempt to use traditional machine learning techniques, namely, Support Vector Machine and Random Forest, delivered strong pixel misclassifications due to the above-mentioned challenges. The use of deep learning for image classification considerably reduced this kind of misclassification error; however, our attempt to train a single deep learning model using the training chips from the flight campaigns during which the reeds were in the phenological maturity stage in order to classify the corresponding orthomosaics using the same generic model was unsuccessful. Not only were the performance metrics significantly lower for this model, the classification results were weak. Strong noise occurred in certain areas, described as "pepper effects" by [36]. Large areas of changing light conditions were generally misclassified, and transition areas between land cover classes appeared in straight edges rather than smooth lines. As a consequence, we trained an individual model for each orthomosaic. This approach, described in Section 3.1, achieved satisfactory results in terms of performance metrics compared to related studies [36,45,46]. The individual models were good at merging intra-class variation into one class as well as at distinguishing between classes. Even changes in the light intensity of the images due to changing sunlight conditions, which the authors of [46] stated as a key challenge, did not influence the classification results of the affected orthomosaics.

While reed ecosystems such as the reed belt of Lake Neusiedl are very valuable wetlands for nature conservation, they are difficult to access and should generally not be entered; remote sensing is an excellent tool to circumvent these concerns. As such, UAV data were used to determine the height, status, and density of reed stands in the lake [47,48]. Other studies have mostly used satellite data to separate reed beds from other vegetation in wetlands (see, e.g., [49,50]), while other studies have used airborne laser scanning to map the extent of reed wetlands (see, e.g., [9,12,51,52]). These studies investigated the respective reed ecosystems only once in a growing season. In addition, airborne laser scanning is highly costly compared to using a UAV. There have been studies mapping salt marshes, including reed ecosystems, with satellite data along the coast and comparing the classification results

between the years; see, e.g., [53]. The evaluation of reed bed changes in [54] showed that changes were induced by management, i.e., reed mowing. In general, satellite data offer lower resolution, and can involve difficulties with cloud cover compared to remote sensing via drone. The height and greenness of vegetation in a floodplain partly covered with reed was studied with several UAV flights per year in [55]. Higgisson et al. [56] illustrated that the structure of the reeds was detectable by a CNN. Our study showed that drone (UAV) remote sensing combined with deep learning is a powerful tool for surveying and classifying reed beds of wetlands in high detail. High-resolution images were obtained several times within a single growing season, allowing the phenology of the reed plant *Phragmites australis* to be observed. We were able to determine the extent of the reed stands as well as the changes in the surrounding areas, such as water and sediment areas, which were induced by the decrease in the water level of the lake due to drought conditions.

4.1. Model Prediction

As input for model training, we fully labeled a subset of eight square-shaped areas on each orthomosaic using the semi-automated image annotation workflow described in Section 2.3.1. These labeled ground truth areas summed to only 4% of the entire study area, and the model prediction yielded favourable results for land cover classification despite the expected challenges stated above. We assumed that it would be crucial to cover the various expressions of each class in the training data; thus, the selection of training areas was carried out with great care. To assess the quality of the model prediction, we manually labeled a representative test area and compared it with the classification results for the same area. The error map in Figure 7 shows that the differences between model prediction and the labeled test area occurred almost exclusively along the class boundaries, where different reasons for pixel misclassification could be identified.
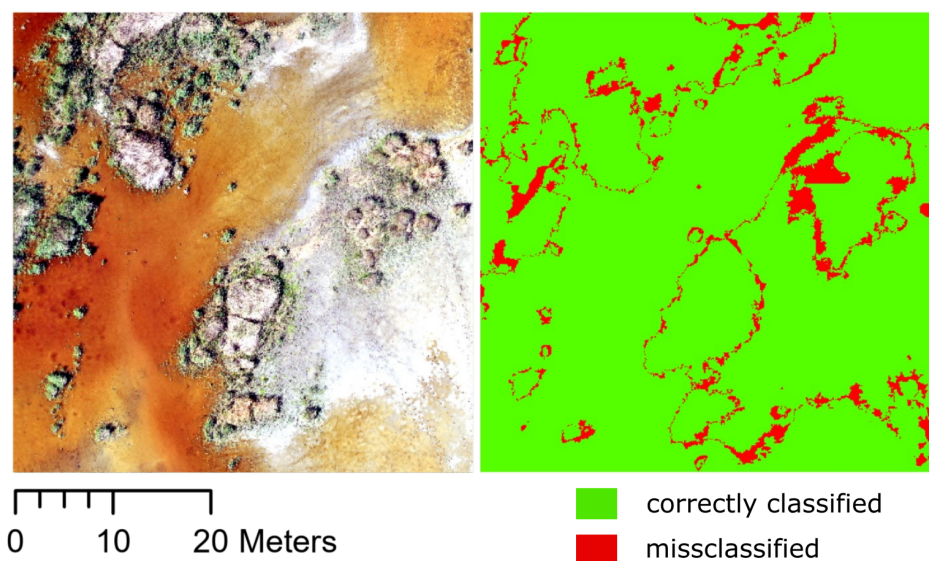
Figure 7. Classification performance of a deep learning model visualized in an error map, showing the difference between labeled test data and the model prediction in a reed ecosystem. Misclassification occurred primarily along class boundaries, especially in transition zones with sparse reed vegetation or very shallow waters, as well as in heavily shaded areas.

First, class boundaries resulting from model prediction ran more smoothly than the class boundaries resulting from the image annotation workflow, which can be considered a negligible error. Second, class boundaries were difficult to predict in extensive transition areas, for example, where water level depths were in the centimeter to millimeter range or in areas with sparse reed vegetation. Third, shaded areas were often reported as misclassified even though they may have been more accurate than the ground truth when compared directly to the imagery. This error may contribute to the significantly lower

IoU values for water and sediment in the model performance metrics (see Table 2 and Appendix A), and suggests that preparation of ground truth data must be done with utmost care. Because misclassification occurred primarily along class boundaries, we believe that adding more representative training data from transition zones could further improve model performance. On the other hand, transition zones are inherently difficult to delineate, which poses a challenge when generating training data. Both the OBIA segmentation tool used in this study and the visual interpretation when merging the segmented polygons had limitation in terms of the accuracy of separating classes in the transition zones.

4.2. Spatio-Temporal Variability

The results of the land cover classification show a clear dominance of reed vegetation in the study area. Previous studies showing a decline of aquatic reeds in central Europe during the last decades [52,57,58] do not match our data within one year. The vegetation area recorded a continuous increase from May to September except for a short period from mid-June to the beginning of July 2021. This rebound of vegetation was likely due to the sudden and complete drying of former water pool areas along the northeastern shore (landward) side of the study area. These pools were sparsely overgrown with juvenile reed shoots in spring, and could be detected well as vegetation by the model. When the pools dried out, increased salinity may have contributed to the dying back of juvenile shoots [59], leading to leaf area loss until the plants could no longer be detected as vegetation by the model. It was clear that large water pool areas dried out and became sediment areas during the study period; when the sediment area reached its maximum extent at the end of June, it was more than four times the size of its minimum extent at the end of May. Water areas declined rapidly from the end of May to mid-September, with the exception of a slight increase on 18 August 2021 due to precipitation in the days immediately preceding the UAV flight (about 20 mm [60]). The distribution of area shares hardly changed from the end of September to the end of the study period. The minor decrease in vegetation area within this period suggests that biomass was no longer being built up, reed growth stopped, and reed leaf surfaces shrank slightly due to dehydration and the onset of wilting. Water and sediment areas were stable because water input (precipitation) and evaporation rates were in balance at this time of the year.

The seasonal temporal changes of the water level of Lake Neusiedl and of the reed belt usually occur annually, with a maximum in spring (March/April) and minimum in autumn (September/October) [14]. Therefore, the temporal change of the mosaic of the reed belt consisting of reed stands, water, and open sediment areas occurs annually due to the change in water level even in "normal" years, though of course with a lower extent compared to the results of our study. Because the reed belt has a gradient from land to open water, spatial changes occur at different rates within the reed belt even in "normal" years. Thus, temporal and spatial changes can be observed in "dry" years as well as in "normal" years. Of course, 2021 was an extreme year, with an especially dry autumn, and conditions actually intensified the following year. It may be suspected that a major consequence of the observed changes in "dry" years for the ecosystem of Lake Neusiedl would be a disconnection between reed belt and open water areas, which would alter food webs and have faunistic and biogeochemical consequences, among others. In "wet" years, on the other hand, there would naturally be rather less spreading of the reed stand areas, though water level changes would nevertheless continue over the year. In this context, however, it should be noted that the last "wet" year with high water levels was 2014 [14].

None of the current studies of Lake Neusiedl [5,8–12] have investigated the spatial and temporal pattern of the three wetland classes (reed, water, and sediment) within one year, though they have often compared the extent of the reed belt between two years, for example, 1979 and 2008. Our study is the first to identify open sediment areas as a separate land cover class in the reed belt. Comparing August 2008 [9] with August 2021 of our study, the share of water areas in the reed belt decreased by 3.7% (from 10.7 to 7%), which would be an opposite development from that of 1979 to 2008, and the vegetation coverage

decreased from 88 to 67%. However, Csaplovics et al. [9] surveyed the entire Austrian reed belt and reported only humic water; therefore, it is unclear whether the lake water of the channels is included in the water areas of the reed belt, as it is not shown as separate class. In contrast to [5,12,13], we observed no die-back sites in our study site for the period from May to November 2021.

The entire lake, including the reed belt, experienced a sharp drop in water level in 2021; thus, the decrease in water areas inside the reed belt could be observed in other parts of the reed belt of Lake Neusiedl as well. Therefore, the decline in water areas in our study can be generalized to an extent to the entire reed belt of Lake Neusiedl. However, because the reed stands vary in age and structure depending on usage/management (west side) or no usage (east side) (see e.g., [9]), and some even include reed stands that have died back (see [5,13]), the increase in reed area within the reed belt cannot be generalized to all areas. Nevertheless, this study shows exemplary temporal and spatial changes in the three wetland classes over the 2021 vegetation period, which was affected by drought conditions.

4.3. Vegetation Phenology

Recently, an example of rapid change in wetland vegetation has been reported from the Rodewiese site, a formerly drained fen on the Baltic coast in NE Germany that was rewetted in 2010. Grassland species that are sensitive to a high water table, such as *Holcus lanatus*, *Potentilla anserina*, and *Trifolium repens*, died back very quickly and were replaced by hydrophytes such as *Lemna* spp. and, with some delay, *Bolboschoenus maritimus*, *Schoenoplectus tabermontanii*, and *Phragmites australis* [61]. Then, in 2018, most of the site that had been covered by water experienced a drought and turned dry, and the fen canopy, with the exception of *Phragmites australis*, disappeared and was colonized by *Tephroseris palustris* and *Ranunculus sceleratus* [62], pioneer species that rapidly spread along nutrient-rich shores of dried-up water bodies [63]. Beyer et al. [62] have pointed out that analogous climate effect feedback generally cannot be anticipated; moreover, van Diggelen et al. [64] and Klimkowska et al. [65] pointed out that in restored fens, water availability, soil, and trophic status were irreversibly altered, along with propagule availability. The conditions experienced in the reed belt of Lake Neusiedl favour *Phragmites australis* as long as the broad ecological amplitude of this reed is not surpassed.

The vegetation in the study area is dominated by reeds, and was tracked using the GCC vegetation index for phenological analysis. The Phenocam data suggest that the phenological time window of the reed stand was well covered in this UAV study. Nevertheless, there is an offset in the GCC data between the Phenocam and the UAV flights in the phenological *Greenup* phase, which is probably due to the different image perspective. Due to the Phenocam's lateral perspective of the reed plants, it naturally detects greening-up earlier than the UAV does from its nadir perspective. However, the UAV covers a much larger spatial area, which of course develops at different rates in the *Greenup* phase from land to open water areas; we have shown the mean and standard deviation of the GCC for the entire study area in Figure 6. The GCC maps in Appendix B show that new vigorous reed shoots grow first along the edges of reed stands and in loosely vegetated areas, leading to an expansion of the vegetation area. In the existing reed mats, shoots break through only gradually, especially in dense areas. When GCC levels peaked in late July, the densest areas of the reed mats were only sparsely overgrown with new reed sprouts; therefore, we do not consider these to be die-back sites.

Phenocam data have the advantages of a lateral perspective and high temporal resolution (hourly/daily basis); however, they are limited to the small area that a single photo is able to cover. On the other hand, while aerial surveys with hundreds of images acquired during a UAV flight campaign can provide detailed information on the spatial development of vegetation over a comparatively large area, they are limited to a lower temporal resolution. Therefore, a combination of both methods can provide complementary analysis.

5. Conclusions

This study aimed to investigate the spatial and temporal changes in the reed belt of Lake Neusiedl under intensive drought conditions. For this purpose, a set of 10 SfM-derived orthomosaics from UAV imagery collected over the 2021 growing season was created. The high-resolution orthomosaics served as a basis to detect changes in land cover and to reveal phenological development. We have demonstrated a semi-automated procedure for generating fully labeled ground truth data for deep learning image segmentation in the context of land cover classification of a wetland. The results of this study underline the strong ability of deep learning models to extract complex features from high-resolution imagery. However, our unsuccessful attempt to train a generic model using training data from multiple flight campaigns encountered limitations. The classification maps revealed an enormous decline in water areas within the reed belt, with a simultaneous increase in sediment areas during the investigation period. Reed vegetation, on the other hand, increased at a nearly constant rate throughout the growing season due to vigorous reed growth along existing reed stands and in loosely vegetated areas, as identified by the GCC maps. While the results of our study can be generalized to the entire reed belt of Lake Neusiedl to a certain extent, the findings may not be applicable to other ecosystems with different environmental factors. This study provides a detailed dataset which can be used to assess the habitat diversity of the reed belt or its ecosystem productivity. In particular, the generated land cover maps may serve as ground truth data for upscaling to more coarsely grained sensor data such as satellite imagery.

Data Availability Statement: Data are available from the PHAIDRA Repository https://doi.org/10.25365/phaidra.397.

Conflicts of Interest: The authors declare no conflict of interest.

Abbreviations

The following abbreviations are used in this manuscript:

APOS	Austrian Positioning Service
CNN	Convolutional Neural Network
DOY	Day of the Year
EC	Eddy Covariance
FN	False Negative
FP	False Positive
GCC	Green Chromatic Coordinates
GCP	Ground Control Points
GNSS	Global Navigation Satellite System
GPU	Graphics Processing Unit
GSD	Ground Sampling Distance

| IoU	Intersection over Union
LCC	Land Cover Classification
LTER	Long-Term Ecological Research
OA	Overall Accuracy
OBIA	Object-Based Image Analysis
RGB	Red–Green–Blue
RMSE	Root Mean Square Error
ROI	Region of Interest
RTK	Real-Time Kinematics
SD	Standard Deviation
SfM	Structure from Motion
TP	True Positive
UAV	Unmanned Aerial Vehicle

Appendix A

Table A1. Detailed table of deep learning parameters and performance metrics. Ten CNN models were trained for land cover classification of UAV imagery for tracking a reed ecosystem over a vegetation period.

| Orthomosaic Date	Image Chips Used for Training	Learning Rate	Accuracy of Last Epoch	Precision			Recall			F1-Score			IoU		
				Vegetation	Water	Sediment	Vegetation	Water	Sediment	Vegetation	Water	Sediment	Vegetation	Water	Sediment
2021-05-05	1621	0.0004	0.945	0.958	0.967	0.892	0.941	0.946	0.952	0.950	0.956	0.921	0.851	0.837	0.629
2021-05-26	1642	0.0010	0.948	0.972	0.918	0.927	0.964	0.945	0.908	0.968	0.931	0.918	0.920	0.847	0.575
2021-06-18	1537	0.0010	0.958	0.977	0.959	0.931	0.965	0.917	0.975	0.971	0.938	0.953	0.924	0.731	0.784
2021-07-07	1574	0.0005	0.935	0.960	0.936	0.868	0.955	0.939	0.899	0.958	0.938	0.883	0.910	0.766	0.662
2021-07-27	1696	0.0008	0.939	0.948	0.878	0.944	0.957	0.912	0.924	0.952	0.895	0.934	0.887	0.476	0.801
2021-08-18	1642	0.0008	0.936	0.964	0.908	0.909	0.951	0.867	0.955	0.958	0.887	0.932	0.905	0.639	0.797
2021-09-10	1533	0.0005	0.950	0.951	0.952	0.947	0.964	0.906	0.951	0.958	0.928	0.949	0.890	0.603	0.835
2021-09-29	1706	0.0005	0.937	0.952	0.904	0.931	0.962	0.915	0.906	0.957	0.909	0.918	0.906	0.543	0.747
2021-10-20	1720	0.0005	0.939	0.958	0.923	0.906	0.953	0.953	0.899	0.955	0.938	0.903	0.904	0.689	0.680
2021-11-06	1741	0.0002	0.939	0.945	0.940	0.922	0.961	0.927	0.899	0.953	0.933	0.910	0.892	0.723	0.693
Mean	1641	0.0006	0.943	0.958	0.929	0.918	0.957	0.923	0.927	0.958	0.925	0.922	0.899	0.685	0.720
SD	71	0.0003	0.007	0.010	0.026	0.023	0.007	0.024	0.027	0.006	0.020	0.020	0.020	0.115	0.081

Appendix B
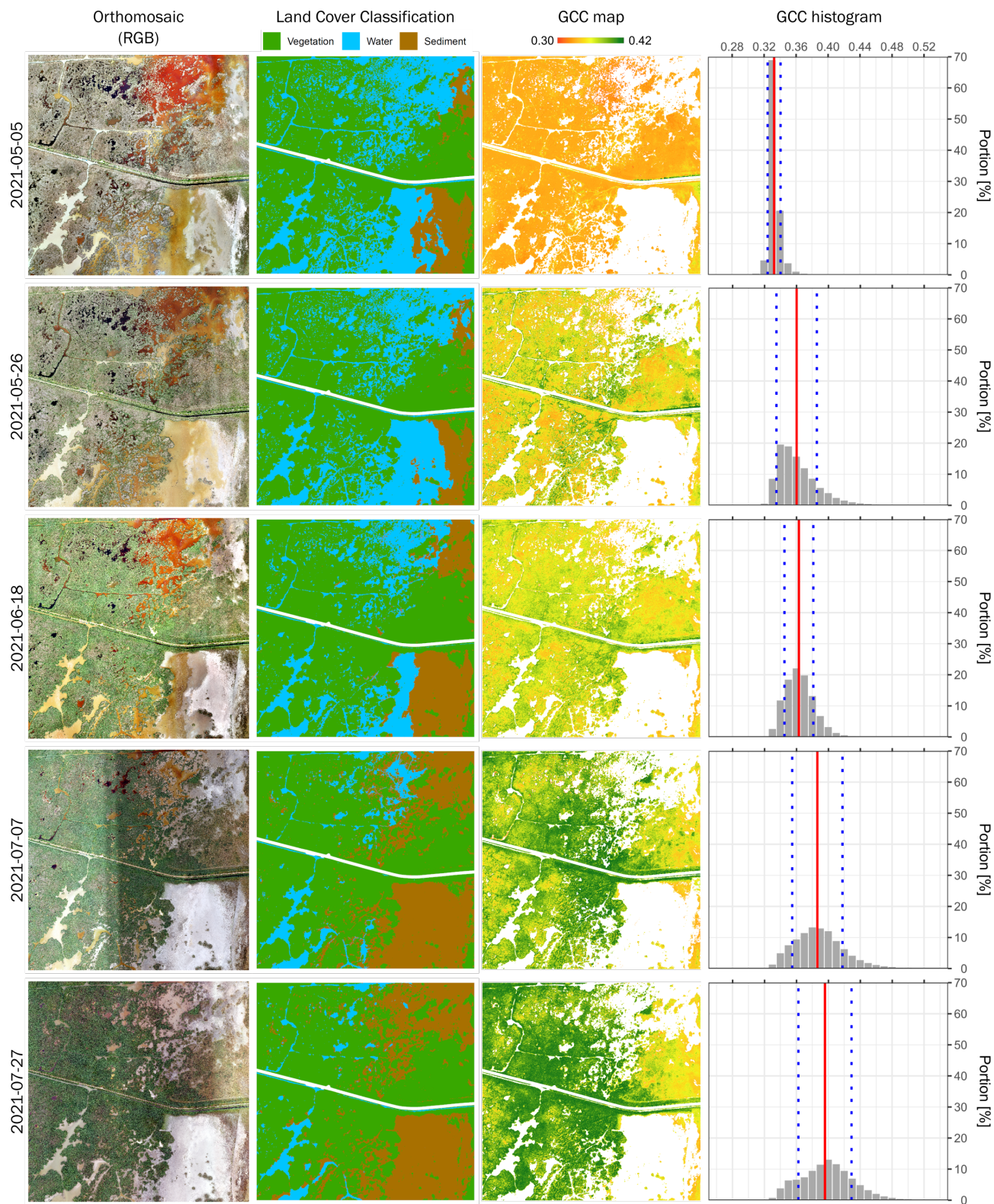
Figure A1. Spatio-temporal development of the study area in the reed ecosystem of Lake Neusiedl from May to July 2021. The mean GCC (red solid line) and the SD (blue dotted lines) of each flight date are shown in the GCC histogram.
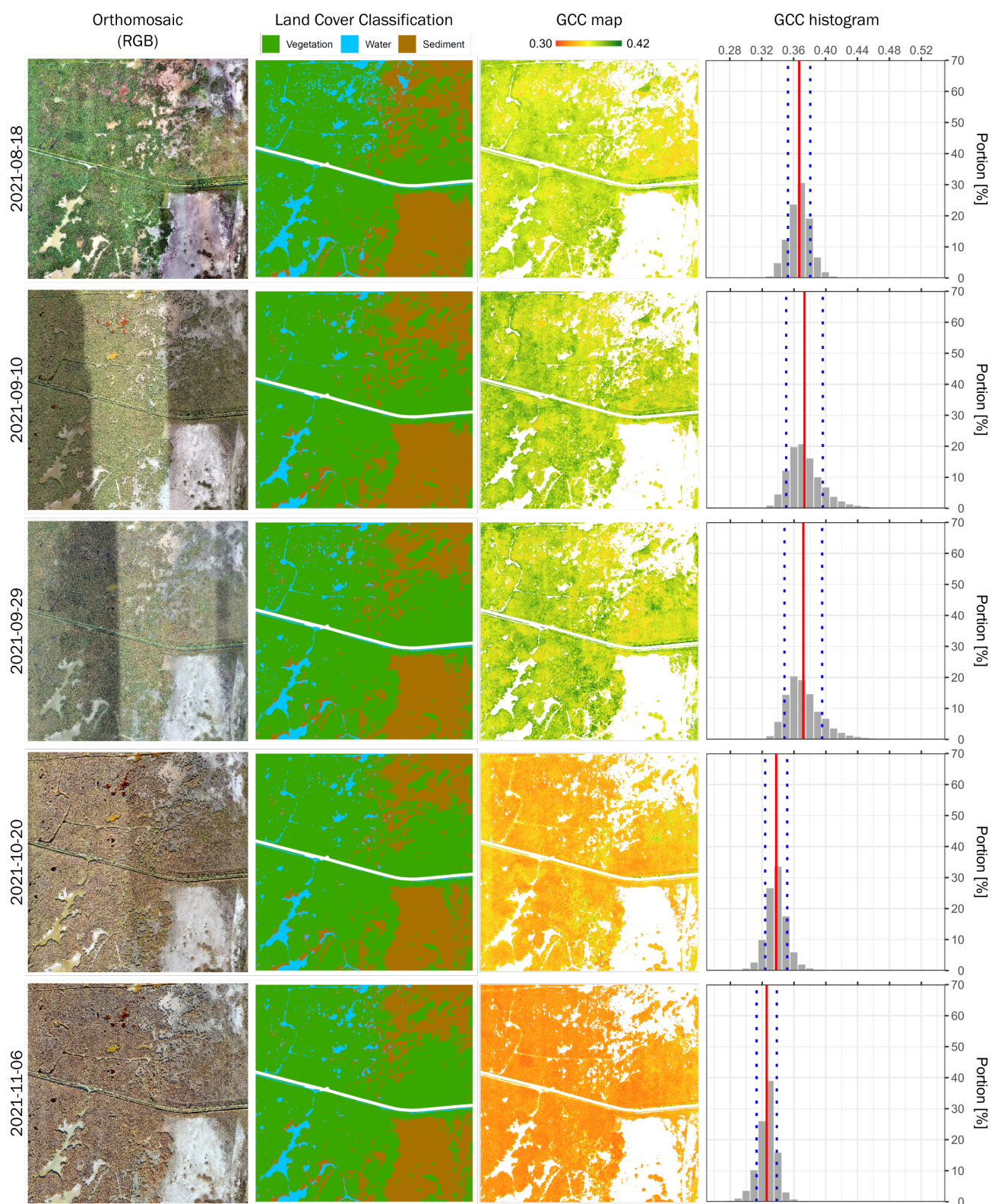
Figure A2. Spatio-temporal development of the study area in the reed ecosystem of Lake Neusiedl from August to November 2021. The mean GCC (red solid line) and the SD (blue dotted lines) of each flight date are shown in the GCC histogram.

References

1. Mitsch, W.J.; Bernal, B.; Hernandez, M.E. Ecosystem services of wetlands. *Int. J. Biodivers. Sci. Ecosyst. Serv. Manag.* **2015**, *11*, 1–4. [CrossRef]
2. Čížková, H.; Kučera, T.; Poulin, B.; Květ, J. Ecological Basis of Ecosystem Services and Management of Wetlands Dominated by Common Reed (Phragmites australis): European Perspective. *Diversity* **2023**, *15*, 629. [CrossRef]
3. Kallasvuo, M.; Lappalainen, A.; Urho, L. Coastal reed belts as fish reproduction habitats. *Boreal Environ. Res.* **2011**, *16*, 1–14.
4. Yu, G.A.; Li, Z.; Yang, H.; Lu, J.; Huang, H.Q.; Yi, Y. Effects of riparian plant roots on the unconsolidated bank stability of meandering channels in the Tarim River, China. *Geomorphology* **2020**, *351*, 106958. [CrossRef]
5. Nemeth, E.; Dvorak, M. Reed die-back and conservation of small reed birds at Lake Neusiedl, Austria. *J. Ornithol.* **2022**, *163*, 683–693. [CrossRef]
6. Mirtl, M.; Bahn, M.; Battin, T.; Borsdorf, A.; Dirnböck, T.; Englisch, M.; Erschbamer, B.; Fuchsberger, J.; Gaube, V.; Grabherr, G.; et al. *Research for the Future LTER-Austria White Paper—On the Status and Orientation of Process Oriented Ecosystem Research, Biodiversity and Conservation Research and Socio-Ecological Research in Austria*; Technical Report; LTER-Austria Series; LTER: Vienna, Austria, 2015; Volume 2, ISBN 978-3-9503986-1-8. Available online: https://www.lter-austria.at (accessed on 5 August 2023).
7. Díaz-Delgado, R.; Cazacu, C.; Adamescu, M. Rapid Assessment of Ecological Integrity for LTER Wetland Sites by Using UAV Multispectral Mapping. *Drones* **2019**, *3*, 3. [CrossRef]
8. Csaplovics, E. Interpretation von Farbinfrarotbildern: Kartierung von Vegetationsschäden in Brixlegg; Schilfkartierung Neusiedler See. *Geowiss. Mitteilungen* **1982**, *23*, 178.
9. Csaplovics, E.; Schmidt, J. Schilfkartierung Neusiedler See: Ausdehnung und Struktur der Schilfbestände des Neusiedler Sees—Projektmanagement, Erfassung und Kartierung des österreichischen Anteiles durch Luftbildklassifikation. 2011. Available online: https://naturschutzbund.at/files/bgl_homepage/projekte/lebensraeume/anlagen/AbschlussberichtSchilfkartierung.pdf (accessed on 5 August 2023).
10. Nemeth, E.; Dvorak, M.; Knoll, T.; Kohler, B.; Mühlbacher, S.; Werba, F. Managementplan für den Neusiedler See als Teil des Europaschutzgebiets Neusiedler See—Nordöstliches Leithagebirge. 2014. Available online: https://www.burgenland.at/fileadmin/user_upload/Natura2000_MP__NeusiedlerSee_web.pdf (accessed on 5 August 2023).
11. Csaplovics, E.; Nemeth, E. Airborne Optical Imaging in Support of Habitat Ecological Monitoring of the Austrian Reed Belt of Lake Neusiedl. In Proceedings of the GISScience RSGIS4HQ, Vienna, Austria, 23–25 September 2014; pp. 163–167. Available online: https://rsgis4hq.geo.tuwien.ac.at/fileadmin/editors/RSGIS4HQ/proceedings/RSGIS4HQ_Csaplovics.pdf (accessed on 5 August 2023)
12. Márkus, I.; Király, G. A Fertő magyarországi nádasainak minősítése, osztályozása és térképezése (Qualification, classification and mapping of the reed stands of the Hungarian part of Lake Fertő). In *Monografikus Tanulmányok a Fertő és a Hanság vidékéről. (Monographic Studies of Lake Fertô and Hanság Area)*; Fertô–Hanság Nemzeti Park Igazgatóság, Szaktudás Kiadó Ház: Budapest, Hungary, 2012; pp. 73–81.
13. Dinka, M.; Ágoston-Szabó, E.; Szeglet, P. Comparison between biomass and C, N, P, S contents of vigorous and die-back reed stands of Lake Fertő/Neusiedler See. *Biologia* **2010**, *65*, 237–247. [CrossRef]
14. Hackl, P.; Ledolter, J. A Statistical Analysis of the Water Levels at Lake Neusiedl. *Austrian J. Stat.* **2023**, *52*, 87–100. [CrossRef]
15. Wolfram, G.; Herzig, A. Nährstoffbilanz Neusiedler See. *Wien. Mitteilungen* **2013**, *228*, 317–338.
16. Hammer, U.T. *Saline Lake Ecosystems of the World*; Junk: Dordrecht, The Netherlands, 1986; p. 616.
17. Soja, G.; Züger, J.; Knoflacher, M.; Kinner, P.; Soja, A.M. Climate impacts on water balance of a shallow steppe lake in Eastern Austria (Lake Neusiedl). *J. Hydrol.* **2013**, *480*, 115–124. [CrossRef]
18. Steiner, G.M.; Englmaier, P.; Fink, M.; Grünweis, F.; Höfner, I.; Korner, I.; Ströhle, A.; Wolf, W. Mittelpunkte der Moorflächen aus dem Moorschutzkatalog (Steiner et al. 1992), 1992. Bundesministerium für Gesundheit und Umweltschutz, Wien. Available online: https://www.data.gv.at/katalog/de/dataset/moorschutzkatalog_1992_points (accessed on 5 August 2023)
19. DJI. Mavic 2 Technische Daten. Available online: https://www.dji.com/at/mavic-2/info (accessed on 25 May 2023).
20. Trimble R1—Datasheet, Model 2 GNSS SYSTEMS. Available online: https://geospatial.trimble.com/sites/geospatial.trimble.com/files/2021-07/022516-332B_TrimbleR10-2_DS_USL_0721_LR.pdf (accessed on 25 May 2023).
21. Villanueva, J.K.S; Blanco, A.C. Optimization of ground control point (GCP) configuration for unmanned aerial vehicle (UAV) survey using structure from motion (SfM). *Int. Arch. Photogramm. Remote. Sens. Spat. Inf. Sci.* **2019**, *XLII-4/W12*, 167–174. [CrossRef]
22. BEV. Bundesamt für Eich- und Vermessungswesen. 2019. Available online: https://www.bev.gv.at/ (accessed on 25 May 2023).
23. Westoby, M.J.; Brasington, J.; Glasser, N.F.; Hambrey, M.J.; Reynolds, J.M. 'Structure-from-Motion' photogrammetry: A low-cost, effective tool for geoscience applications. *Geomorphology* **2012**, *179*, 300–314. . [CrossRef]
24. Deliry, S.I.; Avdan, U. Accuracy of Unmanned Aerial Systems Photogrammetry and Structure from Motion in Surveying and Mapping: A Review. *J. Indian Soc. Remote Sens.* **2021**, *49*, 1997–2017. [CrossRef]
25. Pix4D Documentation. 2023. Available online: https://support.pix4d.com/hc/en-us/sections/360003718571-How-to-step-by-step-instructions (accessed on 25 May 2023).
26. Shen, F.; Zeng, G. Semantic image segmentation via guidance of image classification. *Neurocomputing* **2019**, *330*, 259–266. [CrossRef]
27. ESRI Inc. *ArcGIS Pro*, Version 3.0.3; ESRI Inc.: Redlands, CA, USA, 2022.
28. ESRI. Deep Learning Libraries for ArcGIS Pro 3.0.3. 2022. Available online: https://github.com/Esri/deep-learning-frameworks.git (accessed on 25 May 2023).

29. Tong, X.Y.; Xia, G.S.; Lu, Q.; Shen, H.; Li, S.; You, S.; Zhang, L. Land-cover classification with high-resolution remote sensing images using transferable deep models. *Remote Sens. Environ.* **2020**, *237*, 111322. [CrossRef]

30. Zhang, X.; Han, L.; Han, L.; Zhu, L. How Well Do Deep Learning-Based Methods for Land Cover Classification and Object Detection Perform on High Resolution Remote Sensing Imagery? *Remote Sens.* **2020**, *12*, 417. [CrossRef]

31. Volpi, M.; Tuia, D. Dense Semantic Labeling of Subdecimeter Resolution Images With Convolutional Neural Networks. *IEEE Trans. Geosci. Remote Sens.* **2017**, *55*, 881–893. [CrossRef]

32. Chen, L.C.; Zhu, Y.; Papandreou, G.; Schroff, F.; Adam, H. Encoder-Decoder with Atrous Separable Convolution for Semantic Image Segmentation. *arXiv* **2018**, arXiv:1802.02611.

33. Zhao, W.; Du, S. Learning multiscale and deep representations for classifying remotely sensed imagery. *ISPRS J. Photogramm. Remote Sens.* **2016**, *113*, 155–165. [CrossRef]

34. Pashaei, M.; Kamangir, H.; Starek, M.J.; Tissot, P. Review and Evaluation of Deep Learning Architectures for Efficient Land Cover Mapping with UAS Hyper-Spatial Imagery: A Case Study Over a Wetland. *Remote Sens.* **2020**, *12*, 959. [CrossRef]

35. Rahman, M.A.; Wang, Y. Optimizing Intersection-Over-Union in Deep Neural Networks for Image Segmentation. In *Advances in Visual Computing*; Bebis, G., Boyle, R., Parvin, B., Koracin, D., Porikli, F., Skaff, S., Entezari, A., Min, J., Iwai, D., Sadagic, A., et al., Eds.; Series Title: Lecture Notes in Computer Science; Springer International Publishing: Cham, Switzerland, 2016; Volume 10072, pp. 234–244. [CrossRef]

36. Zheng, J.Y.; Hao, Y.Y.; Wang, Y.C.; Zhou, S.Q.; Wu, W.B.; Yuan, Q.; Gao, Y.; Guo, H.Q.; Cai, X.X.; Zhao, B. Coastal Wetland Vegetation Classification Using Pixel-Based, Object-Based and Deep Learning Methods Based on RGB-UAV. *Land* **2022**, *11*, 2039. [CrossRef]

37. Anagnostis, A.; Tagarakis, A.C.; Kateris, D.; Moysiadis, V.; Sørensen, C.G.; Pearson, S.; Bochtis, D. Orchard Mapping with Deep Learning Semantic Segmentation. *Sensors* **2021**, *21*, 3813. [CrossRef] [PubMed]

38. ESRI. ArcGIS API for Python—Arcgis.learn Module. 2022. Available online: https://developers.arcgis.com/python/api-reference/arcgis.learn.toc.html#deeplab (accessed on 25 May 2023).

39. Sonnentag, O.; Hufkens, K.; Teshera-Sterne, C.; Young, A.M.; Friedl, M.; Braswell, B.H.; Milliman, T.; O'Keefe, J.; Richardson, A.D. Digital repeat photography for phenological research in forest ecosystems. *Agric. For. Meteorol.* **2012**, *152*, 159–177. [CrossRef]

40. Filippa, G.; Cremonese, E.; Migliavacca, M.; Galvagno, M.; Folker, M.; Richardson, A.D.; Tomelleri, E. *Package 'Phenopix': Process Digital Images of a Vegetation Cover*; R Package Version 2.4.2; R Core Team: Vienna, Austria, 2020. Available online: https://cran.rstudio.com/web/packages/phenopix/phenopix.pdf (accessed on 25 May 2023).

41. Filippa, G.; Cremonese, E.; Migliavacca, M.; Galvagno, M.; Forkel, M.; Wingate, L.; Tomelleri, E.; Di Morra Cella, U.; Richardson, A.D. Phenopix: A R package for image-based vegetation phenology. *Agric. For. Meteorol.* **2016**, *220*, 141–150. [CrossRef]

42. R Core Team. *R: A Language and Environment for Statistical Computing: R Foundation for Statistical Computing*; Version 4.2.2; R Core Team: Vienna, Austria, 2022. Available online: https://www.R-project.org/ (accessed on 25 May 2023).

43. Dowle, M.; Srinivasan, A. *Data.table: Extension of 'Data.Frame'*; R Package Version 1.14.8; R Core Team: Vienna, Austria, 2023. Available online: https://CRAN.R-project.org/package=data.table (accessed on 25 May 2023).

44. Wickham, H. *ggplot2: Elegant Graphics for Data Analysis*; Springer: New York, NY, USA, 2016. Available online: https://ggplot2.tidyverse.org (accessed on 25 May 2023).

45. Al-Najjar, H.A.H.; Kalantar, B.; Pradhan, B.; Saeidi, V.; Halin, A.A.; Ueda, N.; Mansor, S. Land Cover Classification from fused DSM and UAV Images Using Convolutional Neural Networks. *Remote Sens.* **2019**, *11*, 1461. [CrossRef]

46. Bhatnagar, S.; Gill, L.; Ghosh, B. Drone Image Segmentation Using Machine and Deep Learning for Mapping Raised Bog Vegetation Communities. *Remote Sens.* **2020**, *12*, 2602. [CrossRef]

47. Meneses, N.C.; Brunner, F.; Baier, S.; Geist, J.; Schneider, T. Quantification of Extent, Density, and Status of Aquatic Reed Beds Using Point Clouds Derived from UAV–RGB Imagery. *Remote Sens.* **2018**, *10*, 1869. [CrossRef]

48. Meneses, N.C.; Baier, S.; Reidelstürz, P.; Geist, J.; Schneider, T. Modelling heights of sparse aquatic reed (Phragmites australis) using Structure from Motion point clouds derived from Rotary- and Fixed-Wing Unmanned Aerial Vehicle (UAV) data. *Limnologica* **2018**, *72*, 10–21. [CrossRef]

49. Villa, P.; Laini, A.; Bresciani, M.; Bolpagni, R. A remote sensing approach to monitor the conservation status of lacustrine Phragmites australis beds. *Wetl. Ecol. Manag.* **2013**, *21*, 399–416. [CrossRef]

50. Davranche, A.; Poulin, B.; Lefebvre, G. Reedbed monitoring using classification trees and SPOT-5 seasonal time series. In Proceedings of the International Symposium on Advanced Methods of Monitoring Reed Habitats in Europe, Illmitz, Austria, 25–26 November 2010; pp. 15–29. Available online: https://hal.science/hal-00692542 (accessed on 5 August 2023).

51. Zlinszky, A. Mapping and conservation of the reed wetlands on Lake Balaton. Ph.D. Thesis, Eötvös Loránd University, Budapest, Hungary, 2013.

52. Dienst, M.; Schmieder, K.; Ostendorp, W. Dynamik der Schilfröhrichte am Bodensee unter dem Einfluss von Wasserstandsvariationen (Effects of water level variations on the dynamics of the reed belts of Lake Constance). *Limnologica* **2004**, *34*, 29–36. [CrossRef]

53. Sun, C.; Li, J.; Liu, Y.; Zhao, S.; Zheng, J.; Zhang, S. Tracking annual changes in the distribution and composition of saltmarsh vegetation on the Jiangsu coast of China using Landsat time series–based phenological parameters. *Remote Sens. Environ.* **2023**, *284*, 113370. [CrossRef]

54. Tiškus, E.; Vaičiūtė, D.; Bučas, M.; Gintauskas, J. Evaluation of common reed (Phragmites australis) bed changes in the context of management using earth observation and automatic threshold. *Eur. J. Remote Sens.* **2023**, *56*, 2161070. [CrossRef]

55.　van Iersel, W.; Straatsma, M.; Addink, E.; Middelkoop, H. Monitoring height and greenness of non-woody floodplain vegetation with UAV time series. *ISPRS J. Photogramm. Remote Sens.* **2018**, *141*, 112–123. [CrossRef]

56.　Higgisson, W.; Cobb, A.; Tschierschke, A.; Dyer, F. Estimating the cover of Phragmites australis using unmanned aerial vehicles and neural networks in a semi–arid wetland. *River Res. Appl.* **2021**, *37*, 1312–1322. [CrossRef]

57.　Nechwatal, J.; Wielgoss, A.; Mendgen, K. Flooding events and rising water temperatures increase the significance of the reed pathogen Pythium phragmitis as a contributing factor in the decline of Phragmites australis. *Hydrobiologia* **2008**, *613*, 109–115. [CrossRef]

58.　Ostendorp, W. 'Die-back' of reeds in Europe—A critical review of literature. *Aquat. Bot.* **1989**, *35*, 5–26. [CrossRef]

59.　Lissner, J.; Schierup, H.H. Effects of salinity on the growth of Phragmites australis. *Aquat. Bot.* **1997**, *55*, 247–260. [CrossRef]

60.　Wasserportal Burgenland. Niederschlag: Illmitz-Biologische Station. 2023. Available online: https://wasser.bgld.gv.at/hydrographie/der-niederschlag/illmitz-biologische-station (accessed on 25 May 2023).

61.　Koch, M.; Koebsch, F.; Hahn, J.; Jurasinski, G. From meadow to shallow lake: Monitoring secondary succession in a coastal fen after rewetting by flooding based on aerial imagery and plot data. *Mires Peat* **2017**, *19*, 1. [CrossRef]

62.　Beyer, F.; Jansen, F.; Jurasinski, G.; Koch, M.; Schröder, B.; Koebsch, F. Drought years in peatland rewetting: Rapid vegetation succession can maintain the net CO_2 sink function. *Biogeosciences* **2021**, *18*, 917–935. [CrossRef]

63.　Fukarek, F.; Henker, H.; Berg, C. *Flora von Mecklenburg-Vorpommern: Farn-und Blütenpflanzen*; Weissdorn-Verlag: Jena, Germany, 2006.

64.　Van Diggelen, R.; Middleton, B.; Bakker, J.; Grootjans, A.; Wassen, M. Fens and floodplains of the temperate zone: Present status, threats, conservation and restoration. *Appl. Veg. Sci.* **2006**, *9*, 157–162. [CrossRef]

65.　Klimkowska, A.; Van Diggelen, R.; Grootjans, A.P.; Kotowski, W. Prospects for fen meadow restoration on severely degraded fens. *Perspect. Plant Ecol. Evol. Syst.* **2010**, *12*, 245–255. [CrossRef]